Separation and Purification Technology 412 (2026) 139558

Contents lists available at ScienceDirect

Separation and Purification Technology

journal homepage: www.elsevier.com/locate/seppur

# Efficient dynamic integrated carbon capture and dry reforming of methane powered by magnetic induction heating

Jianhao Chen, Zhao Li, Wenkang Xu, Hao-Fan Wang, Yonghai Cao, Hongjuan Wang, Hao Yu *

*School of Chemistry and Chemical Engineering, Guangdong Provincial Key Lab of Green Chemical Product Technology, South China University of Technology, Guangzhou 510641, China*

ARTICLE INFO

Editor: Yeshui Zhang

*Keywords:*
ICCU-DRM
Magnetic induction heating
Tri-functional materials
Temperature swing

ABSTRACT

Calcium-looping-based integrated carbon capture and dry reforming of methane (ICCU-DRM) is a representative dynamic integrated carbon capture and utilization process, in which $CO_2$ capture at lower temperatures and in situ conversion of calcium carbonate at higher temperatures are coupled within one system. However, the temperature mismatch between these two stages inevitably introduces repeated heating and cooling, leading to substantial non-productive thermal consumption and limiting overall process efficiency. Here, we introduce magnetic induction heating (MIH) into ICCU-DRM and construct a tri-functional FeCoNi@CaAl material platform that integrates $CO_2$ capture, DRM catalysis and magnetothermal heating within one material. Compared with conventional resistance furnace heating, MIH enables direct internal heat generation within the tri-functional material (TFM) bed, markedly accelerating start-up and temperature swing between the capture and conversion stages. As a result, the total cycle time is shortened from about 91 min to 52 min, while the fraction of non-productive time decreases from 49.5% to 11.5%. The MIH-driven system delivers higher $CO_2$ capture and $H_2$ production normalized by the total electricity-input during ten cycles, indicating improved energy utilization in the electrified ICCU-DRM process. This work highlights the potential of coupling multifunctional material design with MIH to reduce non-productive thermal-transition periods in high-temperature dynamic ICCU operation.

## 1. Introduction

Integrated carbon capture and utilization (ICCU), which combines $CO_2$ capture and subsequent conversion within a single process, has emerged as a promising strategy for improving the overall efficiency of $CO_2$ utilization. Compared with conventional stepwise carbon capture and utilization routes, ICCU can reduce process complexity, avoid intermediate $CO_2$ purification or compression, and strengthen the spatial coupling between $CO_2$ capture and catalytic conversion sites [1–4]. Among various ICCU pathways, calcium-looping-based integrated carbon capture and dry reforming of methane (ICCU-DRM) is particularly appealing because it enables the cyclic conversion of captured $CO_2$ with $CH_4$, another major greenhouse gas, into synthesis gas [5–7]. This process therefore offers a potential route for coupling $CO_2$ abatement with the production of value-added C1-derived chemical intermediates.

Considerable efforts have been devoted to the development of dual-functional materials (DFMs) for ICCU-DRM. In typical CaO-based DFMs, CaO or CaO-derived phases act as $CO_2$ capture components, while transition metals or noble metals, such as Ru, Ni, Co and Fe, serve as catalytic sites for methane activation and reforming reactions [8–15]. Meanwhile, Al-, Mg-, Zr- and Ce-containing phases have been introduced to stabilize CaO, regulate metal–support interactions and improve cyclic durability [16–19]. These studies have substantially advanced the material-level integration of $CO_2$ capture and conversion functions. More recently, the design of multifunctional ICCU materials has moved beyond simple capture–catalysis coupling, with additional emphasis on

*Abbreviations and symbols:* AMF, Alternating magnetic field; ICCU-DRM, Calcium-looping-based integrated carbon capture and dry reforming of methane; TFM, Tri-functional material; DRM, Dry reforming of methane; GC, Gas chromatography; MIH, Magnetic induction heating; RFH, Resistance furnace heating; SLP, Specific loss power; TPD, Temperature-programmed desorption; TPR, Temperature-programmed reduction; XRD, X-ray diffraction; $C_p$, Specific heat capacity; $F$, Volumetric flow rate; $m_{TFM}$, Mass of tri-functional material; $m_{magn}$, Mass of magnetic material; $m_s$, Total mass of dispersion; $n_{CO2,cap}$, Apparent $CO_2$ capture amount; $R_i$, Reacted amount of component i per unit material mass; $S_{CO}$, CO selectivity; $t$, Reaction time; $V_m$, Molar volume of gas at standard conditions; $X_{CH4}$, $CH_4$ conversion; $Y_i$, Formation rate of product $i$ per unit material mass and per unit time; $y_i$, Mole fraction of component $i$.

* Corresponding author.
*E-mail address:* yuhao@scut.edu.cn (H. Yu).

https://doi.org/10.1016/j.seppur.2026.139558
Received 21 May 2026; Received in revised form 19 July 2026; Accepted 28 July 2026
Available online 29 July 2026
1383-5866/© 2026 Published by Elsevier B.V.

structural stabilization, redox regulation, coke resistance and cyclic durability [20–25].

Despite these advances, the performance of ICCU-DRM is not determined solely by the intrinsic $CO_2$ uptake capacity or the steady-state DRM activity of the material. Different from continuous catalytic reactions, ICCU-DRM proceeds through repeated capture, purge and conversion stages, in which the materials undergo periodic changes in gas atmosphere and temperature. For CaO-based systems, $CO_2$ capture is generally favored at relatively lower temperatures, whereas carbonate decomposition and methane reforming require higher temperatures to achieve efficient $CO_2$ release and syngas formation [26,27]. Therefore, a dynamic temperature swing is often required. Under conventional resistance furnace heating (RFH), heat is transferred from the external furnace to the reactor wall and then to the packed bed, resulting in slow thermal response, considerable thermal inertia and extended non-productive heating periods. As a result, even if the local coupling between capture and conversion sites is improved, the process-level penalty associated with repeated temperature transitions can still limit the overall efficiency of ICCU-DRM [28].

Electrified heating technologies provide an opportunity to address this thermal-management limitation in dynamic catalytic processes. Microwave heating can enable rapid volumetric heating through dielectric interaction, but the heating behavior is highly dependent on the dielectric properties of the material bed and the electromagnetic-field distribution, which may cause temperature non-uniformity or scale-dependent hot spots [29]. Joule heating can generate heat efficiently through electrically conductive pathways, but it usually requires direct electrical contact, continuous conductive networks or specially designed reactor structures, which may complicate cyclic operation of packed beds [30]. By contrast, magnetic induction heating (MIH) produces heat directly within magnetic or electrically conductive components under an alternating magnetic field through hysteresis loss, relaxation loss and eddy-current dissipation [31,32]. This contactless internal-heating mode allows the heat-generating materials to be incorporated into the reactive material itself, making MIH well suited for cyclic temperature-swing processes that require rapid and repeated thermal transitions [33].

Introducing MIH into ICCU-DRM imposes additional requirements on material design. The material should not only integrate $CO_2$ capture and DRM catalytic functions, but also exhibit sufficient magnetic and magnetothermal responses to enable efficient internal heating under an alternating magnetic field. Accordingly, a tri-functional material capable of combining $CO_2$ capture, methane reforming and magnetothermal heating within one material platform is required. In such a system, heat can be generated directly inside the reactor bed and in close proximity to the domains responsible for carbonate decomposition and reforming reactions, thereby reducing the thermal lag inherent to external heating and improving the dynamic efficiency of cyclic ICCU-DRM operation.

In this work, a tri-functional FeCoNi@CaAl material was developed for MIH-assisted calcium-looping ICCU-DRM. The CaO-based component provides $CO_2$ capture sites, while the Ca—Al oxide framework contributes to structural stabilization and helps maintain the dispersion of metallic species during cyclic operation [34]. The FeCoNi alloy phase is designed to serve dual roles as the DRM catalytic component and the magnetothermal heating component. In particular, Ni and Co contribute to methane activation and reforming reactions [35,36], whereas Fe enhances the magnetic response and electromagnetic energy dissipation under an alternating magnetic field [37]. Through this integrated design, FeCoNi@CaAl enables the coupling of $CO_2$ capture, methane reforming and internal magnetothermal heating within a single material system. The cyclic ICCU-DRM performance of FeCoNi@CaAl was evaluated under both RFH and MIH conditions. In addition to conventional material-level descriptors, including $CO_2$ capture capacity, $CH_4$ conversion, CO selectivity and $H_2$/CO ratio, process-level dynamic indicators such as cycle time, non-productive heating period and electricity-input-normalized $CO_2$ capture and $H_2$ production were further considered. By correlating the capture–conversion behavior with the thermal response of the material under MIH, this study provides a material–process integrated strategy for improving the dynamic efficiency of high-temperature ICCU processes.

## 2. Experimental

### 2.1. Synthesis of tri-functional FeCoNi@CaAl materials

FeCoNi@CaAl composite materials were synthesized by a glucose-assisted hydrothermal co-precipitation method. In a typical synthesis, the corresponding precursor nitrate salts were dissolved in 60 mL of deionized water to form a transparent solution. Glucose (0.06 mol) and urea (0.06 mol) were then added. Glucose was used as an organic additive to regulate precursor formation during the hydrothermal process, while urea served as a homogeneous precipitating agent that gradually released alkaline species upon heating, thereby promoting the co-precipitation of metal ions together with Ca and Al species. After vigorous stirring for 30 min, the solution was transferred into a 100 mL Teflon-lined stainless-steel autoclave and maintained at 180 °C for 12 h. After naturally cooling to room temperature, the resulting precipitate was collected by centrifugation, repeatedly washed with deionized water and ethanol, and dried at 60 °C for 12 h. The obtained precursor was heated to 750 °C with a ramping rate of 2 °C $min^{-1}$ and calcined for 1 h in air, followed by reduction in 20% $H_2/N_2$ at 800 °C for 2 h to obtain the final tri-functional material (TFM). The resulting samples were denoted as FeCoNi@*x*CaAl, Co@*x*CaAl, CoNi@*x*CaAl, and FeCo@*x*-CaAl, where *x* represents the Ca/Al molar ratio in the support.

In the tri-functional material (TFM) design, the nominal mass fractions of Fe, Co, and Ni in the reduced FeCoNi@*x*CaAl were fixed at 15, 25, and 7 wt%, respectively, with a total metal loading of 47 wt%, while the remaining 53 wt% was assigned to the Ca—Al oxide framework. Based on the Ca/Al molar ratio and assuming that Ca and Al exist as CaO and $Al_2O_3$ in the reduced materials, the nominal CaO contents of FeCoNi@3CaAl, FeCoNi@5CaAl and FeCoNi@10CaAl were calculated to be 40.7, 44.8 and 48.6 wt%, respectively. For samples with different Ca/Al ratios, the total metal loading and their relative fractions were kept unchanged, while the Ca/Al molar ratio in the support was adjusted by varying the amounts of $Ca(NO_3)_2{\cdot}4H_2O$ and $Al(NO_3)_3{\cdot}9H_2O$. For the comparison among monometallic, bimetallic, and trimetallic samples, the Ca/Al molar ratio was fixed at 5 and the total metal loading was fixed at 47 wt%, while the metal composition was tuned by varying the amounts of $Fe(NO_3)_3{\cdot}9H_2O$, $Co(NO_3)_2{\cdot}6H_2O$, and $Ni(NO_3)_2{\cdot}6H_2O$. Specifically, the nominal metal fractions were 47.0 wt% Co for Co@5CaAl, 36.6 wt% Co and 10.4 wt% Ni for CoNi@5CaAl, 18.2 wt% Fe and 28.8 wt% Co for FeCo@5CaAl. The nominal CaO content was 44.8 wt%.

### 2.2. Characterizations

X-ray diffraction (XRD) patterns were recorded on a PANalytical X'Pert Powder diffractometer using Cu K$\alpha$ radiation over a 2$\theta$ range of 10–80°. Transmission electron microscopy (TEM, JEM-2100F, JEOL) equipped with energy-dispersive spectroscopy (EDS) was used to analyze the microstructure and elemental distribution of the samples. $H_2$-temperature-programmed reduction ($H_2$-TPR) and $CO_2$-temperature-programmed desorption ($CO_2$-TPD) measurements were carried out on an AutoChem II 2920 chemisorption analyzer (Micromeritics), and $H_2$ consumption and $CO_2$ desorption signals were monitored by the built-in thermal conductivity detector (TCD). Magnetic properties were measured using a LakeShore 7404 vibrating sample magnetometer in a magnetic field range of −2 to 2 T at 303 K, with a sensitivity of $5 \times 10^{-7}$ emu.

The induction-heating capability of the magnetic components was evaluated by the specific loss power (SLP) using a customized MIH device (SPG-06-I), according to Eq. (1):

$$\mathrm{SLP} = C_{p,s} \cdot \frac{\Delta T}{\Delta t} \cdot \frac{m_s}{m_{\mathrm{magn}}} \quad (1)$$

where $C_{p,s}$ is the specific heat capacity of the dispersion medium, which was approximated as that of water, 4.18 J $g^{-1}$ $K^{-1}$; $\Delta T/\Delta t$ is the initial heating rate under the alternating magnetic field; $m_s$ is the total mass of the dispersion, approximated by the mass of water; and $m_{magn}$ is the mass of the magnetic tri-functional material (TFM). The device operated at a frequency of 300 kHz, and the maximum magnetic field strength in the central region was 4.8 kA $m^{-1}$. For each measurement, 25 mg of tri-functional material (TFM) was dispersed in 5 mL of deionized water in a vacuum Dewar vessel positioned at the center of the induction coil. The temperature was monitored using an optical fiber probe inserted into the bottom of the dispersion. Each sample was measured three times, and the average value was used to calculate the SLP (Fig. S1).

### 2.3. ICCU-DRM evaluation under MIH and RFH

The ICCU-DRM performance of tri-functional material (TFM) was evaluated in a fixed-bed quartz reactor with an inner diameter of 8 mm, an outer diameter of 12 mm, and a length of 450 mm. In each experiment, 0.5 g of TFM was loaded and fixed at the center of the reactor using quartz wool. Under resistance furnace heating (RFH), the reactor was placed in the center of a tubular furnace, whereas under magnetic induction heating (MIH), the reactor was positioned at the center of a coil. The MIH reaction evaluation was conducted using a high-frequency induction heating power supply (SPG-06-I, Shenzhen Shuangping Power Supply Technology Co., Ltd., China) with a rated power of 6 kW. The alternating magnetic field was generated by an 8-turn water-cooled hollow copper coil with an inner diameter of 3 cm, operating at a fixed frequency of 300 kHz. During MIH operation, circulating water was used to cool the copper coil, and the quartz reactor was placed at the center of the coil to ensure effective coupling between the alternating magnetic field and the tri-functional material bed. To ensure a consistent temperature-control criterion for the two heating modes, the bed-center temperature was used in both cases. To minimize the eddy-current dissipation of the metallic thermocouple under AMF, a ceramic-encapsulated ultrafine S-type thermocouple was installed. A blank experiment was conducted using 0.5 g of $Al_2O_3$ as a non-inductive filler to calibrate the temperature under MIH. As shown in Fig. S2, the maximum additional temperature rise of the thermocouple is about 10 °C within the current range investigated, which is small enough compared with the reaction temperature in this work. Unless otherwise specified, the temperatures under MIH are all the bed-center temperatures measured by the thermocouple. The key differences between the RFH and MIH reaction configurations are summarized in Table S1.

Before each experiment, 100 mL $min^{-1}$ pure $N_2$ was introduced to remove residual air from the reactor. The tri-functional material (TFM) was then reduced in situ in 100 mL $min^{-1}$ of 20% $H_2/N_2$ by heating from room temperature to 800 °C at a ramping rate of 10 °C $min^{-1}$, followed by holding for 2 h. After reduction, the gas atmosphere was switched to 100 mL $min^{-1}$ pure $N_2$. For single-cycle dynamic-behavior comparison, the ICCU-DRM cycle consisted of a $CO_2$ capture step at 650 °C, followed by 100 mL $min^{-1}$ $N_2$ purging/heating and a DRM conversion step at 700 °C. During the $CO_2$ capture stage, a 10% $CO_2/N_2$ mixture was introduced at 100 mL $min^{-1}$ for 21 min, followed by 100 mL $min^{-1}$ $N_2$ purging for 5 min and heating to 700 °C. The DRM step was then carried out in 100 mL $min^{-1}$ 5% $CH_4/N_2$ for 25 min. For multi-cycle evaluation, after the initial start-up cycle, each subsequent cycle followed a fixed capture-conversion protocol: $CO_2$ capture was performed at 650 °C in 100 mL $min^{-1}$ 10% $CO_2/N_2$ for 11 min, followed by 100 mL $min^{-1}$ $N_2$ purging/heating to 700 °C, and then DRM reaction in 100 mL $min^{-1}$ 5% $CH_4/N_2$ for 8 min. The outlet gas was analyzed online using a gas chromatograph (GC 9790, Fuli, China).

To compare the electricity-input-normalized performance of MIH and RFH, the total electrical energy input over a complete cycle was quantified for both heating modes. Under RFH, the electricity consumption was recorded directly using an inline power meter. Under MIH, the total electrical energy input was obtained by integrating the recorded real-time power signal over time. To ensure comparability, the electrical energy input of both heating modes was quantified over the same cycle period and was then used to analyze the relationships of cumulative $CO_2$ capture and $H_2$ production with electricity input.

To accurately evaluate the actual $CO_2$ consumption of the tri-functional material (TFM) bed during the capture step, a blank experiment was conducted under the same reactor configuration, tri-functional material (TFM) mass, temperature, gas composition, and total flow rate, using 500 mg of quartz sand instead of tri-functional material (TFM). The corresponding dynamic outlet $CO_2$ profile in the absence of $CO_2$ capture was taken as the blank baseline. As schematically illustrated in Fig. S3, this baseline was used to correct the dynamic delay in outlet $CO_2$ response. The apparent $CO_2$ capture amount during the capture step was calculated according to Eq. (2):

$$\mathrm{n}_{\mathrm{CO_2,cap}} = \frac{F}{V_m} \int_0^t \left( y_{\mathrm{CO_2,blank}} - y_{\mathrm{CO_2,sample}} \right) dt \quad (2)$$

where $n_{CO2,cap}$ is the apparent $CO_2$ capture amount, $F$ is the volumetric flow rate, $V_m$ is the molar volume of gas at standard conditions, $y_{CO2,\ blank}$ is the outlet $CO_2$ mole fraction of the blank experiment, and $y_{\mathrm{CO2,\ sample}}$ is the outlet $CO_2$ mole fraction measured in the catalytic experiment.

The mole fraction of component $i$ ($i$ = $H_2$, CO, $CH_4$, and $CO_2$) in the outlet gas was calculated according to Eq. (3):

$$y_i = \frac{n_i}{\sum_j n_j} \times 100\% \quad (3)$$

where $n_i$ is the molar amount of component $i$, and $\sum nj$ is the total molar amount of all detected gas-phase components.

The average production rate of product $i$ and the amount of reacted component $i$ were calculated according to Eqs. (4) and (5), respectively:

$$Y_i = \frac{n_i}{m_{\mathrm{cat}} t} \quad (4)$$

$$R_i = \frac{n_{i,in} - n_{i,out}}{m_{\mathrm{TFM}}} \quad (5)$$

where $Y_i$ (mmol $g^{-1}$ $min^{-1}$) is the formation rate of product $i$ per unit tri-functional material (TFM) mass and per unit time, $R_i$ (mmol $g^{-1}$) is the reacted amount of component $i$ per unit tri-functional material (TFM) mass, $m_{TFM}$ is the tri-functional material (TFM) mass, and $t$ is the duration of the corresponding stage.

For the DRM step, the $CH_4$ conversion, $H_2$/CO ratio, and CO selectivity were defined according to Eqs. (6)–(8):

$$X_{\mathrm{CH_4}} = \frac{n_{\mathrm{CH_4,in}} - n_{\mathrm{CH_4,out}}}{n_{\mathrm{CH_4,in}}} \times 100\% \quad (6)$$

$$\frac{\mathrm{H_2}}{\mathrm{CO}} = \frac{Y_{\mathrm{H_2,DRM}}}{Y_{\mathrm{CO,DRM}}} \quad (7)$$

$$S_{\mathrm{CO}} = \frac{n_{\mathrm{CO,out}}}{n_{\mathrm{CO,out}} + n_{\mathrm{CO_2,out}}} \times 100\% \quad (8)$$

where $X_{CH4}$ is the $CH_4$ conversion during the DRM step; $n_{\mathrm{CH4,in}}$ and $n_{\mathrm{CH4,\ out}}$ are the inlet and outlet cumulative molar amounts of $CH_4$, respectively. $Y_{H2,DRM}$ and $Y_{CO,DRM}$ are the average production rates of $H_2$ and CO during the DRM step; and $S_{CO}$ is the CO selectivity during the DRM step, with $n_{CO,out}$ and $n_{CO2}$,out being the outlet cumulative molar amounts of CO and $CO_2$, respectively.

## 3. Results and discussion

### 3.1. FeCoNi@CaAl tri-functional materials

To meet the coupled requirements of $CO_2$ capture, DRM conversion, and induction heating in the ICCU-DRM cycle, a tri-functional FeCoNi@CaAl material was synthesized by a glucose-assisted hydrothermal co-precipitation route, as illustrated in Fig. 1a. In this material platform, the Ca-based phase serves as the $CO_2$ capture component, the FeCoNi metallic phase is responsible for DRM conversion and induction heating, and the Ca—Al oxide framework provides structural support and helps disperse the metallic components [34].

The XRD results reveal the phase evolution of the samples from calcination to reduction. As shown in Fig. 1d–f, the calcined samples all exhibit distinct diffraction peaks of $CaCO_3$, together with signals assigned to $Fe_3O_4$, $Co_3O_4$, and NiO, indicating that the Ca-based component mainly exists in carbonate form at this stage, whereas Fe, Co, and Ni are present as oxidized species. After $H_2$ reduction, the diffraction peaks corresponding to metal oxides disappear, while peaks of CaO and metallic phases emerge, indicating that the precursor has been converted into a composite system composed of CaO as $CO_2$ absorber and functional metallic phases. The enlarged patterns in the 42° – 46° range further show that FeCoNi@5CaAl exhibits both bcc and fcc alloy-related peaks [38,39], whereas Co@5CaAl and CoNi@5CaAl mainly display a single alloy structure, suggesting that the coexistence of three metals alters the alloy-phase formation after reduction. FeCo@5CaAl mainly shows a bcc-alloy-like diffraction feature, although some peak asymmetry is still observed.

STEM-EDS analysis further provides microscopic structural information for the reduced FeCoNi@5CaAl sample. As shown in Fig. 1b, Fe, Co, and Ni are spatially overlapped in local regions, whereas Ca, Al, and O are homogeneously distributed throughout the observed area. The corresponding line-scan result shows that the Fe, Co, and Ni signals rise simultaneously within the particle region, indicating that the three metals mainly exist as alloy particles rather than as separated metal domains (Fig. 1c). Meanwhile, the homogeneous distribution of Ca, Al, and O suggests that the alloy particles remain in close contact with the Ca-based phase and the Ca—Al oxide framework. This spatial arrangement provides the structural basis for subsequent multifunctional cooperation, in which the CaO phase is associated with $CO_2$ capture, while the FeCoNi alloy phase is responsible for $CH_4$ activation and induction heating.

The reducibility of samples with different metal compositions was investigated by $H_2$-TPR. As shown in Fig. 2a, Co@5CaAl exhibits two main reduction peaks at 401 and 564 °C, indicating the presence of at least two kinds of Co species with different reducibility. After introducing Ni, the major reduction peaks of CoNi@5CaAl shift to 308 and 434 °C, suggesting that Ni facilitates the reduction of Co-containing oxide species, likely through altered local alloying environments [40,41]. Fe-containing samples show more pronounced high-

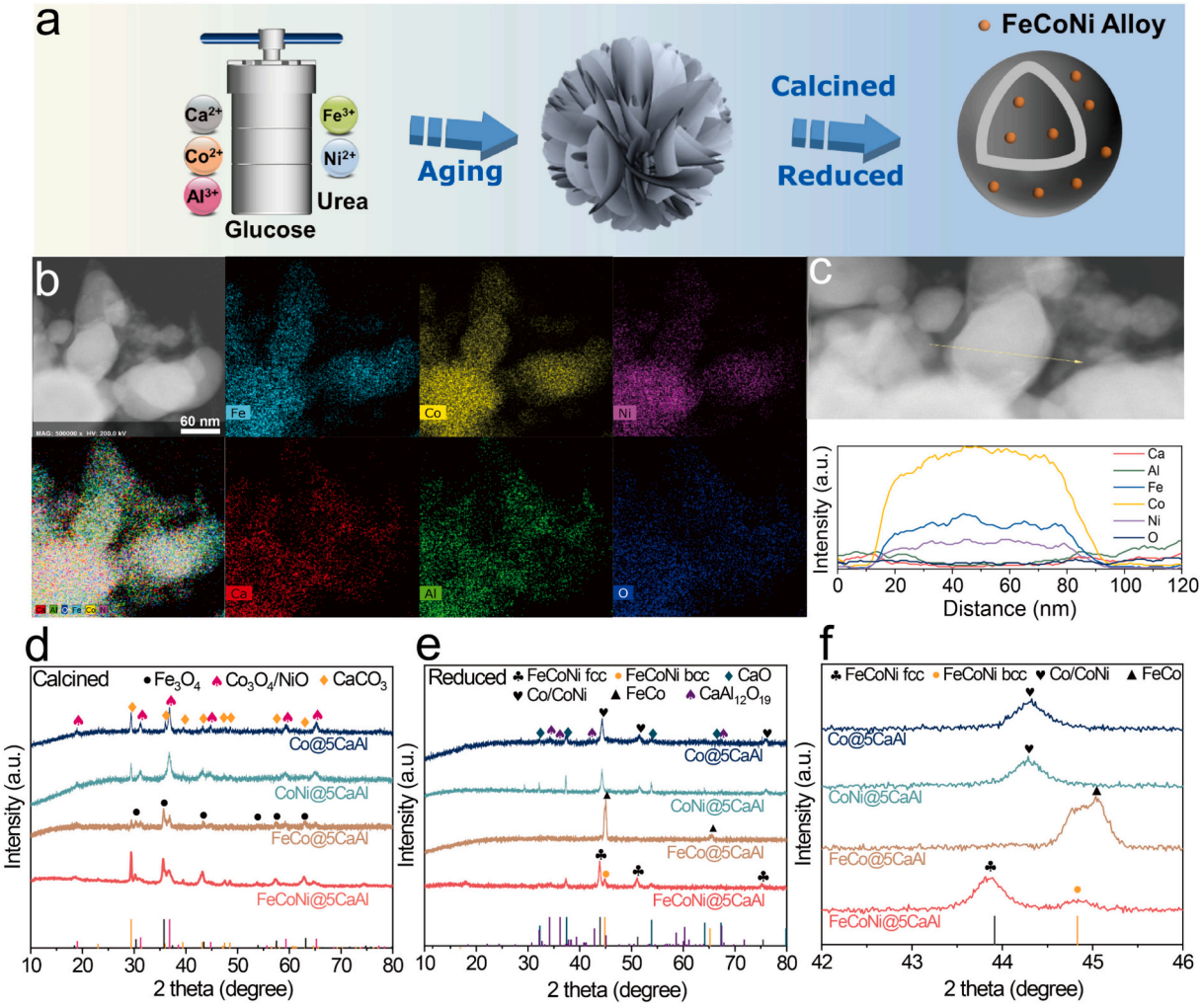


**Fig. 1.** (a) Schematic illustration of the synthesis route of FeCoNi@CaAl. (b) STEM-EDS elemental mapping and (c) line-scan image profiles of reduced FeCoNi@5CaAl. (d) and (e) show the XRD patterns of the calcined and reduced samples, respectively. (f) shows the enlarged XRD patterns in the 42°–46° region of (e).

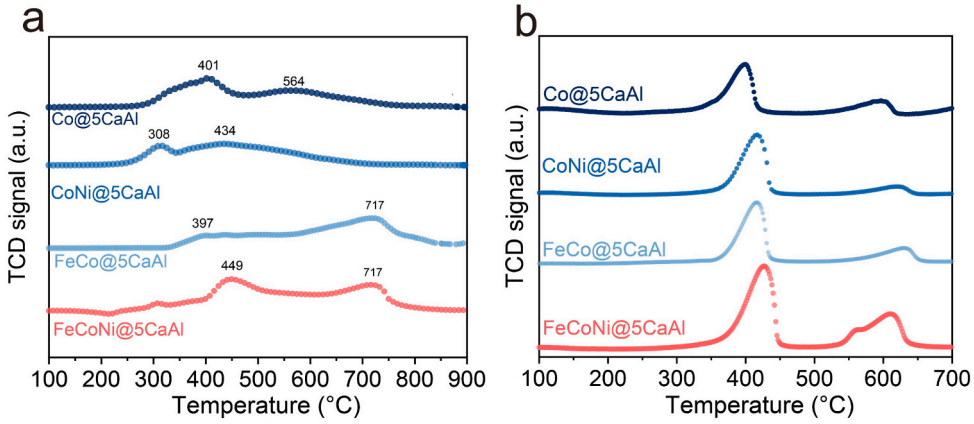


**Fig. 2.** (a) $H_2$-TPR profiles of the calcined tri-functional material (TFM). (b) $CO_2$-TPD profiles of the reduced tri-functional material (TFM).

temperature reduction characteristics. FeCo@5CaAl presents reduction peaks at 397 and 717 °C, whereas FeCoNi@5CaAl shows two major peaks at 449 and 717 °C. The appearance of the high-temperature peak near 717 °C suggests that the introduction of Fe leads to the formation of more difficult-to-reduce species, while the shift of the low-temperature peak from 397 °C in FeCo@5CaAl to 449 °C in FeCoNi@5CaAl indicates that the local chemical environment of the metallic species is further altered when Fe, Co, and Ni coexist [42].

$CO_2$-TPD profiles reflect the differences in basic-site distribution among the samples. As shown in Fig. 2b, all four samples exhibit a main desorption peak at about 400–430 °C, indicating the presence of abundant medium-strength basic sites [43,44]. More obvious differences are observed in the high-temperature region. Co@5CaAl and CoNi@5CaAl show weak high-temperature desorption signals near 600 °C, whereas FeCo@5CaAl exhibits enhanced high-temperature desorption, and FeCoNi@5CaAl displays a stronger and broader desorption band over 500–620 °C. This suggests that the simultaneous incorporation of Fe, Co, and Ni not only preserves medium-strength basic sites, but also generates more strongly adsorbing basic sites capable of stabilizing $CO_2$.

### 3.2. ICCU-DRM performance of FeCoNi@CaAl tri-functional materials

As shown in Fig. 3a, with increasing Ca/Al ratio, the $CO_2$ capture capacity of FeCoNi@*x*CaAl increases from 4.53 to 5.77 and 6.12 mmol $g^{-1}$, indicating that a higher Ca/Al ratio is favorable for increasing the number of accessible capture sites. In contrast, the behavior during the conversion step does not follow the same trend. Fig. 3b shows that the $CH_4$ conversion decreases from 90.94% to 85.61% and 82.20%, whereas the CO selectivity reaches the highest value of 92.70% for the sample with a Ca/Al ratio of 5:1. Fig. 3c further shows that the sample with $x = 3$ gives a relatively high $H_2$ production rate, while the sample with $x$ value of 5 exhibits the highest CO production rate; when the Ca/Al ratio is further increased to 10:1, both rates decrease. These results indicate that a higher $CO_2$ capture capacity does not necessarily lead to superior

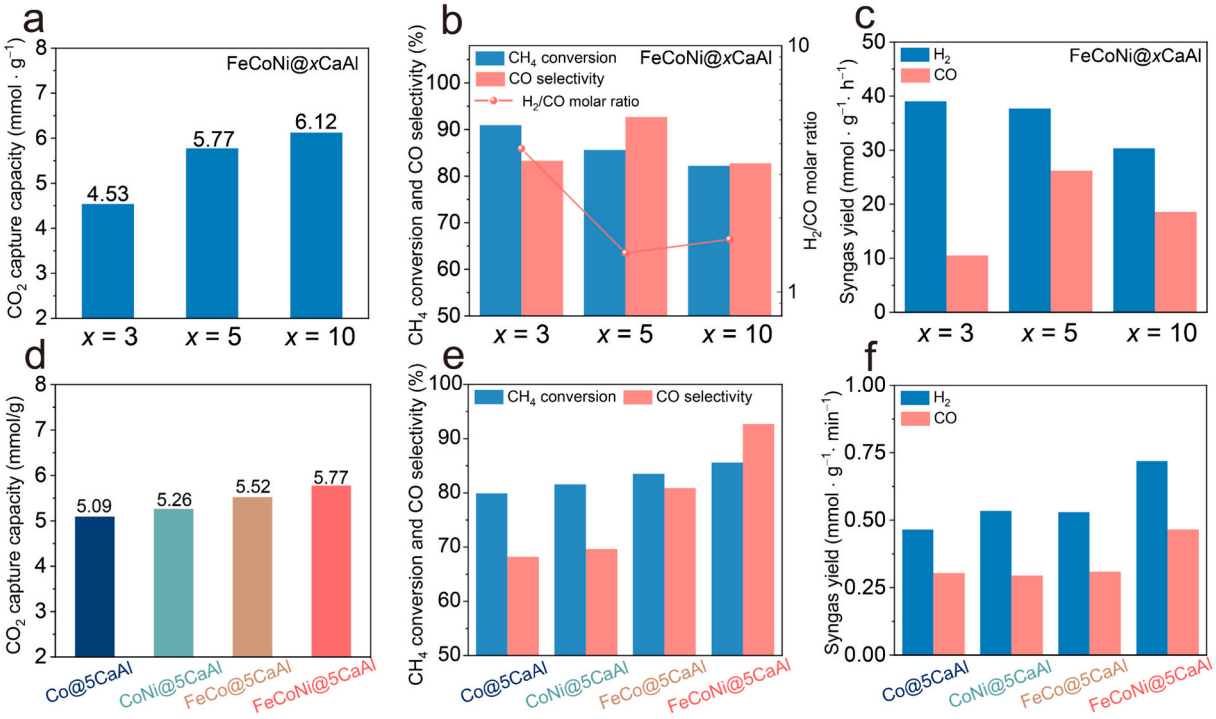


**Fig. 3.** Composition-dependent ICCU-DRM performance of the tri-functional materials. (a) $CO_2$ capture capacity, (b) $CH_4$ conversion, CO selectivity, and $H_2$/CO molar ratio, and (c) syngas yields over FeCoNi@*x*CaAl. (d) $CO_2$ capture capacity, (e) $CH_4$ conversion, CO selectivity, and $H_2$/CO molar ratio, and (f) syngas production rates over Co@5CaAl, CoNi@5CaAl, FeCo@5CaAl, and FeCoNi@5CaAl.

DRM performance. Although FeCoNi@3CaAl gives relatively high $CH_4$ conversion, its CO generation is insufficient, whereas FeCoNi@10CaAl captures more $CO_2$ but does not translate this advantage into higher output during the DRM stage. By comparison, FeCoNi@5CaAl shows a better overall balance among $CO_2$ capture capacity, $CH_4$ conversion, CO selectivity, and syngas production, and was therefore selected as the more suitable support composition. Table S2 compares the material-level performance of representative CaO-based DFMs and ICCU-DRM systems reported in the literature. Most previous studies were conducted under conventional thermal operation and mainly focused on improving $CO_2$ capture capacity, $CH_4$ conversion, syngas yield, or cyclic stability. In comparison, FeCoNi@5CaAl shows a balanced $CO_2$ capture–conversion performance, confirming its suitability as a representative TFM for ICCU-DRM operation. Since such comparison cannot reflect the thermal-transition efficiency of dynamic ICCU-DRM processes, the magnetic and magnetothermal properties of the TFM were further investigated.

Fixing the Ca/Al ratio at 5:1, the effects of metal composition were investigated. As shown in Fig. 3d, the $CO_2$ capture capacities of Co@5CaAl, CoNi@5CaAl, FeCo@5CaAl, and FeCoNi@5CaAl are 5.09, 5.26, 5.52, and 5.77 mmol $g^{-1}$, respectively. Since the Ca/Al ratio is identical for this group of samples, this difference indicates that metal composition also affects the apparent $CO_2$ capture behavior under the present cyclic conditions, likely through its influence on the local environment and utilization of the CaO phase. Fig. 3e and f show that the metal composition exerts a more pronounced influence on the DRM step. Co@5CaAl and CoNi@5CaAl exhibit similar $CH_4$ conversion, but both show relatively low CO selectivity. The introduction of Fe results in the increase of both $CH_4$ conversion and CO selectivity. When Fe, Co, and Ni coexist, FeCoNi@5CaAl delivers the highest $CH_4$ conversion, CO selectivity, and $H_2$ and CO production rates, with the improvement in CO production being particularly notable. These results suggest that, on this material platform, the synergistic effect of the three metals is more favorable for simultaneously promoting $CH_4$ activation and $CO_2$ conversion, thereby enhancing syngas production. Above parametric studies indicate that although FeCoNi@5CaAl is not the best sample in a single performance metric, it achieves the most reasonable overall balance between $CO_2$ capture and DRM conversion. Therefore, FeCoNi@5CaAl was identified as the most suitable tri-functional material for dynamic ICCU-DRM operation.

### 3.3. Magnetic and magnetothermal properties of FeCoNi@CaAl

The magnetic properties and induction-heating behaviors of the tri-functional materials were then examined to evaluate their suitability for rapid temperature swing under MIH. The room-temperature magnetic hysteresis loops are shown in Fig. 4a. All samples exhibit distinct ferromagnetic behavior, indicating that the reduced metallic phases can respond effectively to AMF. Differences in magnetization behavior are also evident. FeCo@5CaAl exhibits the highest saturation magnetization, followed by FeCoNi@5CaAl, whereas CoNi@5CaAl and Co@5CaAl show lower values. This indicates that the introduction of Fe enhances the magnetic responsiveness, while the subsequent incorporation of Ni slightly decreases the magnetization compared with FeCo@5CaAl. The enlarged low-field region in Fig. 4b further shows that FeCoNi@5CaAl has a narrower hysteresis loop and lower coercivity than FeCo@5CaAl does, suggesting that Ni reduces the resistance to magnetization reversal while preserving strong magnetic responsiveness. Overall,

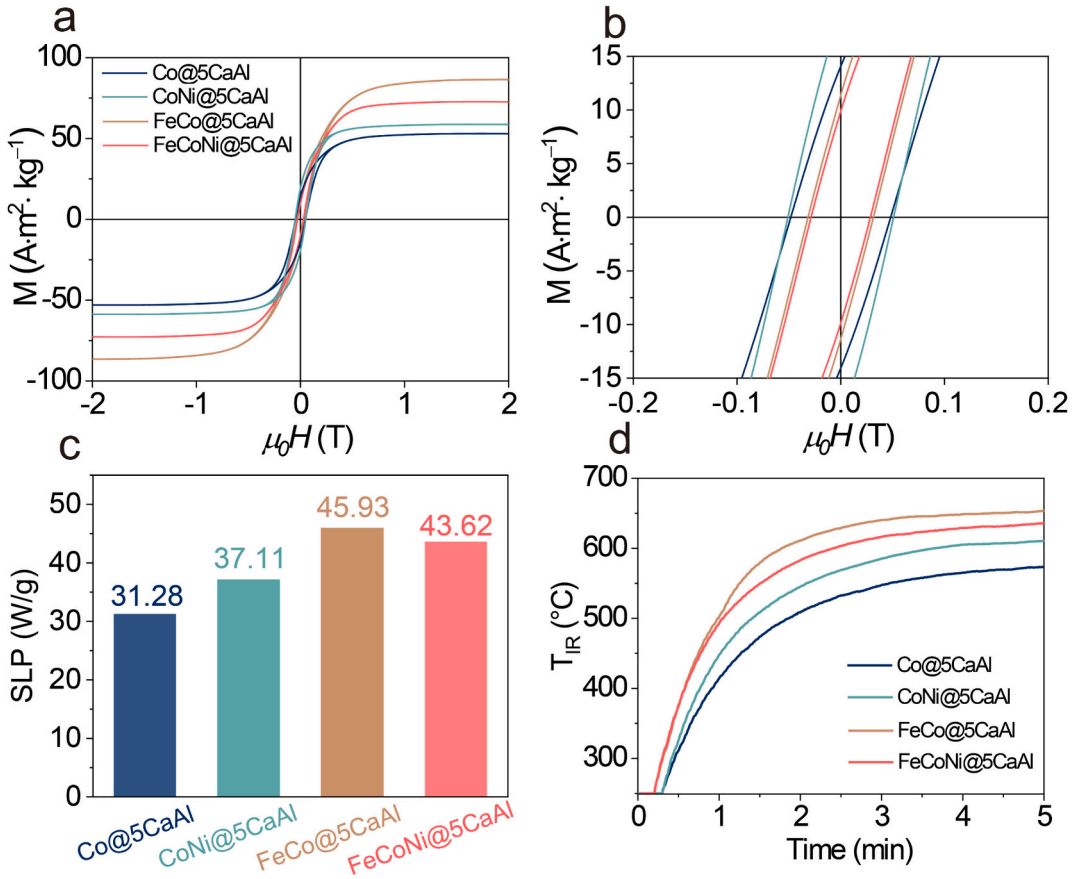


**Fig. 4.** (a) Room-temperature magnetic hysteresis (M–H) loops of Co@5CaAl, CoNi@5CaAl, FeCo@5CaAl and FeCoNi@5CaAl measured under an applied field of ±20 kOe. (b) shows the enlarged low-field region. (c) Calorimetric measurements conducted under an AMF (300 kHz, 3.0 mT). (d) Temperature profiles recorded by an infrared thermometer of Co@5CaAl, CoNi@5CaAl, FeCo@5CaAl and FeCoNi@5CaAl under 6.37 mT.

FeCoNi@5CaAl and FeCo@5CaAl exhibit better magnetic characteristics than Co@5CaAl and CoNi@5CaAl.

To further compare the energy dissipation capability of the samples under an AMF, the SLP values were measured. As shown in Fig. 4c, the SLP values of Co@5CaAl, CoNi@5CaAl, FeCo@5CaAl, and FeCoNi@5-CaAl are 31.28, 37.11, 45.93, and 43.62 W $g^{-1}$, respectively. Overall, the SLP increases after alloying with other metals. The strong ferromagnetism associated with Fe contributes to the highest SLP observed for FeCo@5CaAl. However, the introduction of nickel slightly reduces the SLP of FeCoNi@5CaAl. Combined with the magnetic hysteresis results, these data indicate that the introduction of Fe plays an important role in enhancing electromagnetic energy dissipation, while FeCo-Ni@5CaAl still retains a sufficiently high magnetothermal conversion capability.

The temperature profiles of the samples under MIH are shown in Fig. 4d. All four samples can be rapidly heated within a short time, but their heating rates and final temperatures differ. Overall, FeCo@5CaAl shows the fastest heating and the highest final temperature, followed by FeCoNi@5CaAl, whereas CoNi@5CaAl and Co@5CaAl exhibit lower heating performance. This trend is consistent with the SLP results, indicating a good correspondence between the actual heating behavior and the magnetothermal dissipation capability of the samples. Although FeCo@5CaAl is slightly superior in magnetic and heating properties, FeCoNi@5CaAl still provides sufficiently fast heating and a sufficiently high final temperature to meet the requirement of rapid temperature swing. It should be noted that the infrared temperature profiles in Fig. 4d were used only to compare the relative magnetothermal responses of different TFMs under identical AMF conditions, while the bed-center temperature profiles recorded under actual ICCU-DRM operating conditions are provided in Fig. S4. Considering the superior $CH_4$ conversion, CO selectivity, and syngas generation of FeCoNi@5-CaAl, it was selected as the representative tri-functional material for subsequent comparison between MIH and RFH.

### 3.4. Dynamic cyclic behaviors of ICCU-DRM operated under MIH and RFH

The dynamic behavior of a single run of ICCU-DRM under RFH and MIH was compared (Fig. 5). Under both heating modes, the process consists of a start-up stage from room temperature to the capture temperature, a $CO_2$ capture stage at 650 °C, a temperature-swing stage to 700 °C, and a DRM stage. The primary difference between RFH and MIH in this single-cycle comparison lies in the temperature-response rate and the associated time penalty. Fig. 5a and b show the outlet gas concentration profiles during one cycle under RFH and MIH, respectively. Under both modes, once $CO_2$ is introduced, the outlet $CO_2$ concentration increases gradually during the capture stage, reflecting the dynamic uptake behavior of the bed. After the system is heated to the conversion temperature and switched to the $CH_4$-containing atmosphere, CO and $H_2$ signals begin to appear in the outlet gas, indicating the onset of DRM. In terms of stage sequence, the two heating modes are essentially the same, but the transition between stages is evidently more compact under MIH,

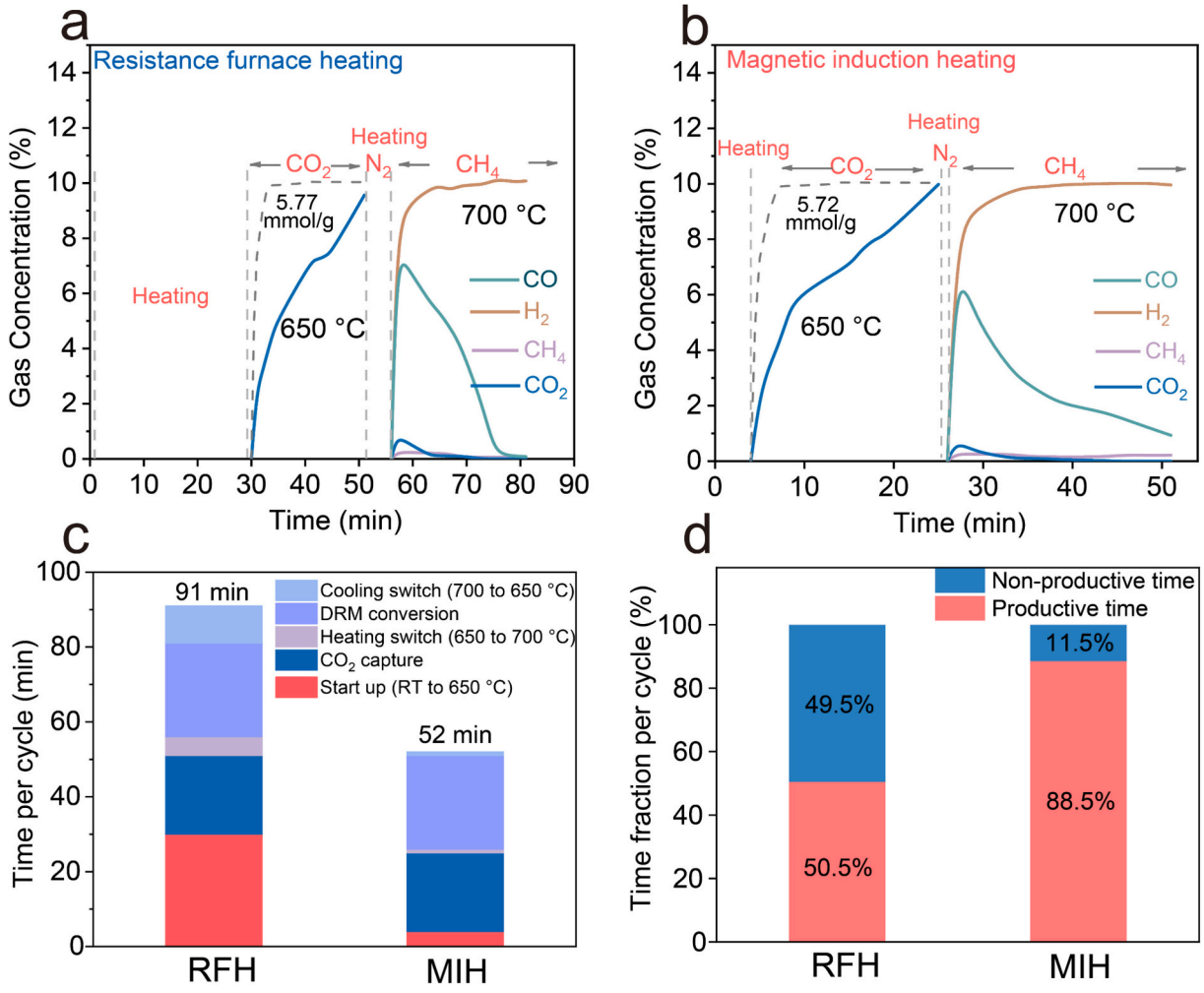


**Fig. 5.** Outlet gas concentration profiles during one ICCU–DRM cycle over FeCoNi@5CaAl under (a) RFH and (b) MIH. (c) Time composition of one cycle. (d) Productive and non-productive time fractions.

especially during start-up and capture-to-conversion switching.

This difference is more directly reflected in the time composition of the cycle. As shown in Fig. 5c, the total duration of a single cycle is about 91 min under RFH and 52 min under MIH, indicating a marked shortening under MIH. Further analysis shows that the preset durations of the $CO_2$ capture stage and the DRM conversion stage are essentially identical under the two heating modes, whereas the difference in total cycle time mainly arises from three segments: heating from room temperature to 650 °C, heating from 650 to 700 °C and cooling from 700 to 650 °C. Under RFH, heating from room temperature to the capture temperature takes about 30 min, whereas under MIH it takes only about 4 min. The switching processes between the two temperatures are also greatly shortened under MIH. These results indicate that the role of MIH is to reduce the thermal transition cost required to realize these stages. When the cycle time is divided into productive and non-productive time, as shown in Fig. 5d, the non-productive fraction under RFH accounts for about 49.5% of the total cycle, which is comparable to the productive fraction. In contrast, under MIH this fraction decreases to 11.5%, while the productive time increases to 88.5%. Therefore, MIH does not merely enhance the heating rate, it changes the time structure of the cycle by reducing the fraction assigned to start-up and temperature swing, allowing a larger fraction of the operating time to be devoted to actual $CO_2$ capture and DRM conversion [29,45].

The significantly improved time efficiency is particularly important for dynamic processes such as ICCU-DRM that repeatedly switch between low-temperature capture and high-temperature conversion, since the process efficiency is determined not only by the apparent output of each reaction stage, but also by the time and energy consumed in the transition between stages. From this perspective, the experimentally observed advantage of MIH in this ICCU-DRM system is mainly reflected in the shorter thermal-transition periods, manifested by the compression of start-up and temperature-swing periods. Under repeated operation, this thermal-management advantage translated into clear benefits in cyclic output and process-level energy utilization. As shown in Fig. 6a, during 10 consecutive cycles, the $CH_4$ conversion under MIH remains at a high level, ranging from 92.03% to 95.13%, without noticeable decline. By contrast, the $CH_4$ conversion under RFH is generally lower, mainly ranging from 79.10% to 86.09%. These results indicate that, under the present cyclic operating conditions and temperature-control criterion, MIH consistently delivers higher conversion output over repeated cycles, suggesting that rapid temperature swing does not compromise the effective conversion capability of the system during the dynamic operation. These results are consistent with the temperature profiles, which show faster and more stable temperature swing under MIH than under RFH (Fig. S4).

The variation in CO selectivity is shown in Fig. 6b. Under MIH, the CO selectivity remains within the range of 89.41%–93.89%, whereas under RFH it also remains relatively stable, ranging from 86.35% to 91.85%. The fluctuation amplitude is limited under both heating modes, but MIH maintains the slightly higher CO selectivity in most cycles. This indicates that MIH delivers higher cyclic conversion output without sacrificing CO selectivity. In addition, the XRD and SEM results before and after cycling show that the main crystalline phases are retained after 10 MIH-driven ICCU-DRM cycles (Fig. S5), while the surface morphology remains relatively stable without essential structural collapse (Fig. S6). To further

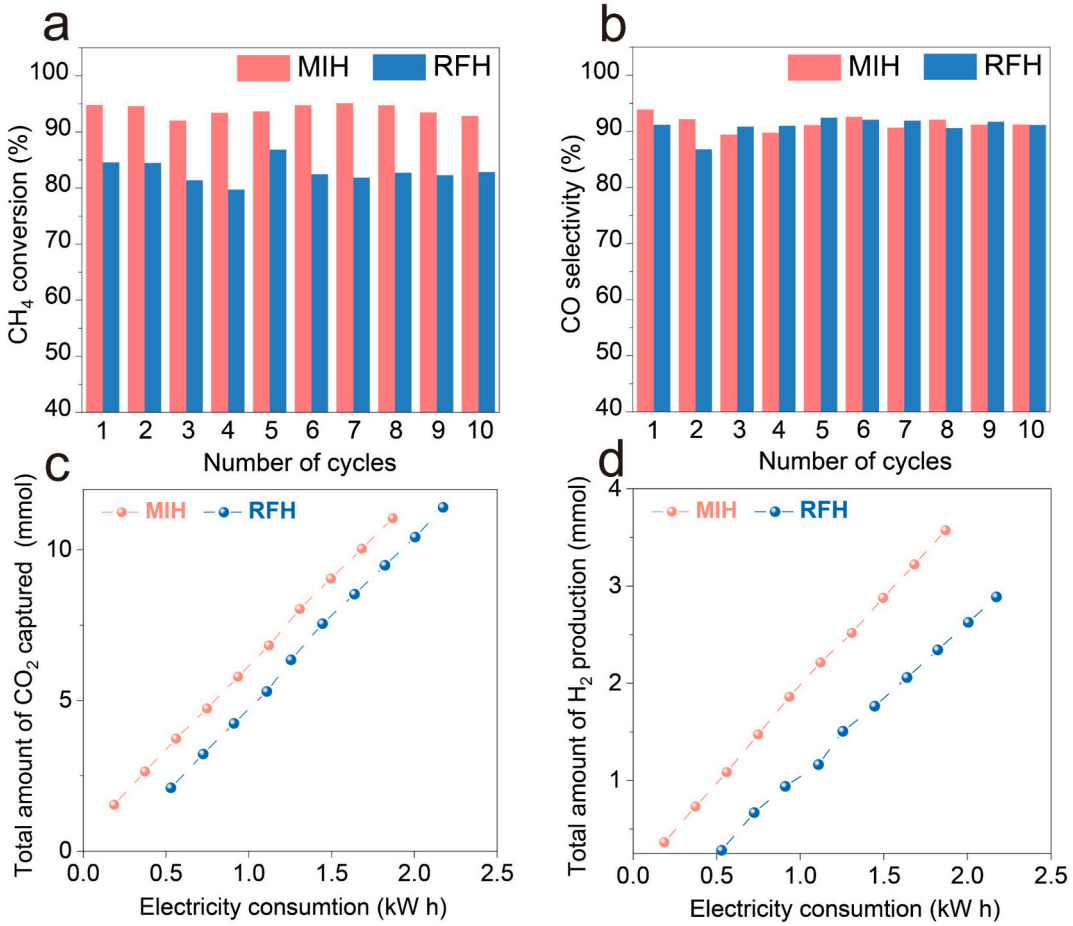


**Fig. 6.** Comparisons of (a) $CH_4$ conversion and (b) CO selectivity during 10 ICCU-DRM operation cycles over FeCoNi@5CaAl under MIH and RFH. After the initial start-up cycle, each subsequent cycle consisted of 10% $CO_2/N_2$ capture at 650 °C for 11 min, followed by $N_2$ purge/heating switching and 5% $CH_4/N_2$ DRM at 700 °C for 8 min. (c) and (d) show the cumulative $CO_2$ uptake and $H_2$ production as functions of total electricity input under MIH and RFH.

evaluate the retention of the $CO_2$ capture function, the spent FeCoNi@5CaAl TFM after 10 MIH-driven ICCU-DRM cycles was subjected to an additional $CO_2$ capture test under the same conditions used for the fresh material. The spent TFM exhibited a $CO_2$ capture capacity of 4.46 mmol $g^{-1}$, corresponding to 77.3% of the initial value of 5.77 mmol $g^{-1}$. Although a moderate decrease in capture capacity was observed, most of the $CO_2$ capture function was retained after repeated capture–conversion cycles. The magnetic hysteresis loop and SLP value of the spent sample after cyclic ICCU-DRM operation were measured to evaluate the magnetothermal stability of FeCoNi@5CaAl. As shown in Fig. S7, the spent FeCoNi@5CaAl retains a clear ferromagnetic response, with only a slight decrease in saturation magnetization compared with the fresh sample. Moreover, the SLP value of the spent FeCoNi@5CaAl remains 40.19 W $g^{-1}$ under the same AMF conditions, indicating that the material still maintains effective magnetic induction heating capability after repeated capture–conversion cycles. These results demonstrate that FeCoNi@5-CaAl maintains not only structural stability but also magnetothermal stability during dynamic MIH-driven ICCU-DRM operation.

The cumulative outcomes were then compared as a function of total electricity input for the two heating modes. As shown in Fig. 6c, with the same total electrical input, MIH consistently gives the higher cumulative $CO_2$ uptake amount than RFH does, indicating a clear advantage in $CO_2$ capture per unit electricity input. Fig. 6d further shows that the cumulative $H_2$ production under MIH is also higher than that under RFH when compared on the same total electricity-input basis. Since Fig. 5 has already shown that the main effect of MIH on a single cycle is the compression of non-productive stages, the cumulative benefits observed in Fig. 6 mainly originate from differences in cycle-time structure and energy-allocation pattern rather than from changes in the preset reaction duration within an individual cycle. This trend is consistent with the shorter non-productive thermal-transition periods under MIH.

Overall, the MIH-driven system shows higher $CO_2$ uptake and $H_2$ production normalized by the recorded electrical input of the heating unit during the tested cycles. This apparent advantage is mainly associated with the shortened start-up and temperature-swing periods, rather than with changes in the prescribed capture or reforming duration. Therefore, MIH provides a practical means to reduce non-productive thermal-transition time in laboratory-scale dynamic ICCU-DRM operation.

### 3.5. Scale-up considerations of MIH-driven ICCU-DRM

Although the present work demonstrates MIH-driven ICCU-DRM at laboratory scale, its scale-up should be considered from the viewpoint of electromagnetic reactor design. Unlike conventional furnace heating, where the thermal response is mainly limited by wall-to-bed heat transfer, MIH generates heat directly inside magnetically responsive components under an alternating magnetic field. Therefore, when magnetic susceptors are properly distributed within the material bed, internal heat generation may help reduce thermal lag and non-productive thermal-transition periods during dynamic operation. From an energy-efficiency perspective, the advantage of MIH is expected to be particularly relevant for cyclic ICCU processes, because repeated heating and cooling can occupy a large fraction of the total cycle time. However, the overall efficiency at larger scale will depend strongly on magnetic-field penetration, coil–reactor coupling efficiency, spatial distribution of the magnetic phase, and bed-scale temperature uniformity [46]. Non-uniform electromagnetic fields may lead to local hot zones or cold zones, while coil cooling and gas switching may introduce additional auxiliary energy consumption. Therefore, future scale-up of MIH-driven ICCU-DRM should focus on structured tri-functional beds, modular induction coil design, and coupled electromagnetic–thermal reactor optimization [47].

## 4. Conclusions

In this work, a magnetic induction heating-driven ICCU-DRM process was proposed to alleviate the non-productive thermal penalty arising from the temperature mismatch between the capture and conversion steps in ICCU-DRM cycling. By constructing a tri-functional FeCoNi@5CaAl material, $CO_2$ capture, DRM catalysis, and MIH were integrated into a single material platform, thereby achieving a coordinated match between material functions and process requirements. The results show that FeCoNi@5CaAl does not rank first in every individual metric, but provides the most balanced overall performance in terms of $CO_2$ capture capacity, DRM conversion behavior, and induction-heating capability. Owing to direct internal heat generation within the tri-functional material (TFM) bed, MIH significantly shortens the start-up and capture-to-conversion switching periods, reducing the total cycle time from about 91 min to 52 min and lowering the fraction of non-productive time from 49.5% to 11.5%. During consecutive cycling, FeCoNi@5CaAl maintains high and stable conversion output under MIH, while simultaneously delivering higher cumulative $CO_2$ capture and $H_2$ production under the same total electricity-input condition. These results suggest that MIH-assisted internal heat generation can improve the apparent time efficiency and electricity-input-normalized output of dynamic ICCU-DRM by compressing non-productive thermal-transition periods under laboratory-scale cyclic conditions.

## CRediT authorship contribution statement

**Jianhao Chen:** Writing – original draft, Visualization, Methodology, Investigation, Formal analysis, Data curation. **Zhao Li:** Validation, Data curation. **Wenkang Xu:** Visualization, Validation. **Hao-Fan Wang:** Supervision, Resources. **Yonghai Cao:** Supervision, Resources. **Hongjuan Wang:** Supervision, Resources. **Hao Yu:** Writing – review & editing, Supervision, Resources, Project administration, Funding acquisition, Conceptualization.

## Declaration of competing interest

The authors declare that they have no known competing financial interests or personal relationships that could have appeared to influence the work reported in this paper.

## Acknowledgements

This work was supported by the Natural Science Foundation of Guangdong Province (No. 2024B1515040016) and Guizhou Provincial Science and Technology Plan Project Natural Science Key Project (ZK [2022] 028).

## Appendix A. Supplementary data

Supplementary data to this article can be found online at https://doi.org/10.1016/j.seppur.2026.139558.

## Data availability

Data will be made available on request.

## References

[1] Z. Xuan Law, Y.-T. Pan, D.-H. Tsai, Calcium looping of $CO_2$ capture coupled to syngas production using Ni-CaO-based dual functional material, Fuel 328 (2022) 125202, https://doi.org/10.1016/j.fuel.2022.125202.
[2] A. Bhaskaran, S.A. Singh, B.M. Reddy, S. Roy, Integrated $CO_2$ capture and dry reforming of $CH_4$ to syngas: a review, Langmuir 40 (2024) 14766–14778, https://doi.org/10.1021/acs.langmuir.4c01852.
[3] J. Li, X. He, R. Hu, Integrated carbon dioxide capture and utilization for the production of $CH_4$, syngas and olefins over dual-function materials, ChemCatChem 16 (2024) e202301714, https://doi.org/10.1002/cctc.202301714.
[4] G. Liu, S. Sun, H. Sun, Y. Zhang, J. Lv, Y. Wang, J. Zeng, Z. Yan, C. Wu, Integrated $CO_2$ capture and utilisation: a promising step contributing to carbon neutrality, Carbon Capture Sci. Technol. 7 (2023) 100116, https://doi.org/10.1016/j.ccst.2023.100116.

[5] J. Hu, P. Hongmanorom, V.V. Galvita, Z. Li, S. Kawi, Bifunctional Ni-ca based material for integrated $CO_2$ capture and conversion via calcium-looping dry reforming, Appl. Catal. B Environ. 284 (2021) 119734, https://doi.org/10.1016/j.apcatb.2020.119734.

[6] M. Peng, R. Han, L. Wei, Y. Wang, Z. Li, H. Yan, G. Han, Q. Liu, Cu promoted Ni-ca dual functional materials for integrated $CO_2$ capture and utilization in $O_2$-containing flue gas: eliminating the delay in the utilization stage, Sep. Purif. Technol. 354 (2025) 129516, https://doi.org/10.1016/j.seppur.2024.129516.

[7] Z.X. Law, D.-H. Tsai, Efficient calcium looping-integrated methane dry reforming by dual functional aerosol ca–Ni–Ce nanoparticle clusters, ACS Sustain. Chem. Eng. 11 (2023) 2574–2585, https://doi.org/10.1021/acssuschemeng.2c06832.

[8] E. García-Bordejé, A.B. Dongil, J. Moral, J.M. Conesa, A. Guerrero-Ruiz, I. Rodríguez-Ramos, Cyclic performance in $CO_2$ capture-methanation of bifunctional Ru with different base metals: effect of the reactivity of $CO_x$ ad-species, J. $CO_2$ Util. 68 (2023) 102370, https://doi.org/10.1016/j.jcou.2022.102370.

[9] J. Hu, P. Hongmanorom, P. Chirawatkul, S. Kawi, Efficient integration of $CO_2$ capture and conversion over a Ni supported $CeO_2$-modified CaO microsphere at moderate temperature, Chem. Eng. J. 426 (2021) 130864, https://doi.org/10.1016/j.cej.2021.130864.

[10] J. Li, C. Gao, Y. Cheng, J. Ran, C. Qin, Calcium looping-based methane reforming for hydrogen and syngas production, Appl. Catal. B Environ. Energy 379 (2025) 125674, https://doi.org/10.1016/j.apcatb.2025.125674.

[11] E. Wang, Z. Zhu, R. Li, J. Wu, K. Ma, J. Zhang, Ni/CaO-based dual-functional materials for calcium-looping $CO_2$ capture and dry reforming of methane: progress and challenges, Chem. Eng. J. 482 (2024) 148476, https://doi.org/10.1016/j.cej.2023.148476.

[12] T. Papalas, D. Lypiridis, A.N. Antzaras, A.A. Lemonidou, Experimental investigation of integrated $CO_2$ capture and conversion to syngas via calcium looping coupled with dry reforming of $CH_4$, Chem. Eng. J. 485 (2024) 149866, https://doi.org/10.1016/j.cej.2024.149866.

[13] B. Shao, Z.-Q. Wang, X.-Q. Gong, H. Liu, F. Qian, P. Hu, J. Hu, Synergistic promotions between $CO_2$ capture and in-situ conversion on Ni-CaO composite catalyst, Nat. Commun. 14 (2023) 996, https://doi.org/10.1038/s41467-023-36646-2.

[14] Y. Zhao, B. Jin, Z. Liang, Synergistic enhanced ca–Fe chemical looping reforming process for integrated $CO_2$ capture and conversion, Ind. Eng. Chem. Res. 59 (2020) 1298–1307, https://doi.org/10.1021/acs.iecr.9b05783.

[15] C. Zhang, Y. Li, Y. Deng, W. Liu, K. Han, Y. Wang, Z. He, J.J. Wu, Hollow submicrospherical Ni/co-promoted CaO/$Ca_{12}Al_{14}O_{33}$ for $H_2$ production from sorption-enhanced water–gas shift with in situ $CO_2$ conversion via $CH_4$ reforming of $CaCO_3$, ACS Catal. 15 (2025) 4208–4228, https://doi.org/10.1021/acscatal.4c07688.

[16] R. Han, S. Xing, Y. Wang, L. Wei, Z. Li, C. Yang, C. Song, Q. Liu, Two birds with one stone: MgO promoted Ni-CaO as stable and coke-resistant bifunctional materials for integrated $CO_2$ capture and conversion, Sep. Purif. Technol. 307 (2023) 122808, https://doi.org/10.1016/j.seppur.2022.122808.

[17] S. Jo, J.H. Woo, T. Nguyen, J.E. Kim, T.Y. Kim, H.-J. Ryu, B. Hwang, J.C. Kim, S. C. Lee, K.L. Gilliard-AbdulAziz, Zr-modified Ni/CaO dual function materials (DFMs) for direct methanation in an integrated $CO_2$ capture and utilization process, Energy Fuel 37 (2023) 19680–19694, https://doi.org/10.1021/acs.energyfuels.3c02935.

[18] L. Wei, R. Han, G. Han, H. Yan, M. Peng, Z. Li, C. Song, Q. Liu, Modulating the evolution of metastable CaO* for the near-theoretical performance breakthrough of Ni/$CeO_2$-CaO in integrated $CO_2$ capture and methanation, Adv. Sci. 12 (2025) 2503086, https://doi.org/10.1002/advs.202503086.

[19] M. Heidari, M. Tahmasebpoor, S.B. Mousavi, C. Pevida, $CO_2$ capture activity of a novel CaO adsorbent stabilized with ($ZrO_2$+$Al_2O_3$+$CeO_2$)-based additive under mild and realistic calcium looping conditions, J. $CO_2$ Util. 53 (2021) 101747, https://doi.org/10.1016/j.jcou.2021.101747.

[20] Y. Shen, S. Sun, F. Lian, Y. Liu, H. Qiu, Engineering robust Ni–CaO interaction using potassium for low-carbon deposition integrated $CO_2$ capture and dry reforming of the methane process, Ind. Eng. Chem. Res. 65 (2026) 2156–2168, https://doi.org/10.1021/acs.iecr.5c04607.

[21] L. Zhang, Y. Zhou, H. Cui, Z. Cheng, Z. Zhou, Performance enhancement of Ni/CaO-$Al_2O_3$ dual-function materials for integrated $CO_2$ capture and conversion via dry reforming of methane, Chem. Eng. Sci. 320 (2026) 122635, https://doi.org/10.1016/j.ces.2025.122635.

[22] X. Zhang, Y. Liao, B. Yang, W. Liu, W. Xu, S. Tian, L. Han, Physically mixed CaO-Ni dual-functional materials for integrated $CO_2$ capture and conversion via $CH_4$ dry reforming: critical role of the proximity, Chem. Eng. J. 532 (2026) 174250, https://doi.org/10.1016/j.cej.2026.174250.

[23] H. Gu, M. Yu, P. Xu, S. Zhao, S. Zhang, Y. Yu, Effects of synthesis method of CaO-Ni/$CeO_2$ dual-functional materials for integrated $CO_2$ capture and $CH_4$ dry reforming, Sep. Purif. Technol. 393 (2026) 137288, https://doi.org/10.1016/j.seppur.2026.137288.

[24] M.A. Elokl, A.G. Ali, A.M. Abdelmohsen, A.A. Taha, A.A. Ashour, S. Elshabrawy, N. K. Allam, Integrated $CO_2$ capture and conversion: dual-functional materials, mechanisms, and pathways to industrial decarbonization, EES Catal. 4 (2026) 522–641, https://doi.org/10.1039/D5EY00322A.

[25] I.S. Omodolor, H.O. Otor, J.A. Andonegui, B.J. Allen, A.C. Alba-Rubio, Dual-function materials for $CO_2$ capture and conversion: a review, Ind. Eng. Chem. Res. 59 (2020) 17612–17631, https://doi.org/10.1021/acs.iecr.0c02218.

[26] R. Jiang, Z. Miao, L. Shen, Study on K-modified ca-based dual-functional materials for carbon capture and in-situ methane dry reforming, J. Energy Inst. 117 (2024) 101847, https://doi.org/10.1016/j.joei.2024.101847.

[27] S. Sun, Y. Wang, Y. Xu, H. Sun, X. Zhao, Y. Zhang, X. Yang, X. Bie, M. Wu, C. Zhang, Y. Zhu, Y. Xu, H. Zhou, C. Wu, Ni-functionalized ca@Si yolk-shell nanoreactors for enhanced integrated $CO_2$ capture and dry reforming of methane via confined catalysis, Appl. Catal. B Environ. Energy 348 (2024) 123838, https://doi.org/10.1016/j.apcatb.2024.123838.

[28] F. He, J. Ma, Q. Hu, J. Wang, Y. Chen, H. Yang, Y. Yang, Enhancing energy efficiency and decarbonization of cement production through integrated calcium-looping and methane dry reforming (CaL-DRM) for in-situ $CO_2$ conversion to syngas, Carbon Capture Sci. Technol. 14 (2025) 100359, https://doi.org/10.1016/j.ccst.2024.100359.

[29] Y. Zhu, K. Liu, Y. Wang, J. Hu, B. Zong, Z. Zhao, X. Gao, C. Wu, Microwave-powered integrated carbon capture and utilisation (ICCU) for methane production with rapid temperature response from minimal thermal inertia, Chem. Eng. J. 500 (2024) 156776, https://doi.org/10.1016/j.cej.2024.156776.

[30] L. Zheng, M. Ambrosetti, E. Tronconi, Joule-heated catalytic reactors toward decarbonization and process intensification: a review, ACS Eng. Au 4 (2024) 4–21, https://doi.org/10.1021/acsengineeringau.3c00045.

[31] F. Varsano, M. Bellusci, A. La Barbera, M. Petrecca, M. Albino, C. Sangregorio, Dry reforming of methane powered by magnetic induction, Int. J. Hydrog. Energy 44 (2019) 21037–21044, https://doi.org/10.1016/j.ijhydene.2019.02.055.

[32] J. Mazarío, S. Ghosh, V. Varela-Izquierdo, L.M. Martínez-Prieto, B. Chaudret, Magnetic nanoparticles and radio frequency induction: from specific heating to magnetically induced catalysis, ChemCatChem 17 (2025) e202400683, https://doi.org/10.1002/cctc.202400683.

[33] V. Poletto Dotsenko, M. Bellusci, A. Masi, D. Pietrogiacomi, F. Varsano, Improving the performances of supported NiCo catalyst for reforming of methane powered by magnetic induction, Catal. Today 418 (2023) 114049, https://doi.org/10.1016/j.cattod.2023.114049.

[34] L. Li, Y. Zhang, J. Feng, S. Zhao, K. Li, Z. Huang, H. Lin, Ni–ca–Al synergistic effect in dual-function materials for integrated $CO_2$ capture and conversion, ACS Sustain. Chem. Eng. 12 (2024) 925–937, https://doi.org/10.1021/acssuschemeng.3c06096.

[35] Z. Wu, B. Yang, S. Miao, W. Liu, J. Xie, S. Lee, M.J. Pellin, D. Xiao, D. Su, D. Ma, Lattice strained Ni-co alloy as a high-performance catalyst for catalytic dry reforming of methane, ACS Catal. 9 (2019) 2693–2700, https://doi.org/10.1021/acscatal.8b02821.

[36] M. Chaghouri, C. Ciotonea, M. Mohamad Ali, M. Marinova, P. Simon, E. Abi-Aad, S. Royer, C. Gennequin, Deposition precipitation derived Ni-co active sites for enhanced dry reforming of methane performances, Catal. Today 429 (2024) 114458, https://doi.org/10.1016/j.cattod.2023.114458.

[37] H. Li, H. Li, F. Yang, Q. Cai, W. Xu, R. Wang, Y. Liu, Electromagnetic absorption properties of Fe*x*CoNi magnetic nano particles, J. Appl. Phys. 135 (2024) 144102, https://doi.org/10.1063/5.0193665.

[38] B. Yang, J. Fang, C. Xu, H. Cao, R. Zhang, B. Zhao, M. Huang, X. Wang, H. Lv, R. Che, One-dimensional magnetic FeCoNi alloy toward low-frequency electromagnetic wave absorption, Nano Micro Lett. 14 (2022) 170, https://doi.org/10.1007/s40820-022-00920-7.

[39] S. Liu, Q. Fan, S. Li, Y. Huang, Y. Chen, H. Liu, Necklace-structured FeCoNi@N-doped porous carbon nanofibers with strong magnetic coupling for high-performance microwave absorption, Compos. Sci. Technol. 272 (2025) 111389, https://doi.org/10.1016/j.compscitech.2025.111389.

[40] S. Li, Y. Wang, L. Gao, Y. Wu, X. Yang, P. Sheng, G. Xiao, Short channeled Ni-co/SBA-15 catalysts for highly selective hydrogenation of biomass-derived furfural to tetrahydrofurfuryl alcohol, Microporous Mesoporous Mater. 262 (2018) 154–165, https://doi.org/10.1016/j.micromeso.2017.11.027.

[41] Y. Turap, I. Wang, T. Fu, Y. Wu, Y. Wang, W. Wang, Co–Ni alloy supported on $CeO_2$ as a bimetallic catalyst for dry reforming of methane, Int. J. Hydrog. Energy 45 (2020) 6538–6548, https://doi.org/10.1016/j.ijhydene.2019.12.223.

[42] T. Zhang, Z. Liu, Y.-A. Zhu, Z. Liu, Z. Sui, K. Zhu, X. Zhou, Dry reforming of methane on Ni-Fe-MgO catalysts: influence of Fe on carbon-resistant property and kinetics, Appl. Catal. B Environ. 264 (2020) 118497, https://doi.org/10.1016/j.apcatb.2019.118497.

[43] D. Liang, Y. Wang, M. Chen, X. Xie, C. Li, J. Wang, L. Yuan, Dry reforming of methane for syngas production over attapulgite-derived MFI zeolite encapsulated bimetallic Ni-co catalysts, Appl. Catal. B Environ. 322 (2023) 122088, https://doi.org/10.1016/j.apcatb.2022.122088.

[44] M.A.A. Aziz, A.A. Jalil, S. Wongsakulphasatch, D.-V.N. Vo, Understanding the role of surface basic sites of catalysts in $CO_2$ activation in dry reforming of methane: a short review, Catal. Sci. Technol. 10 (2020) 35–45, https://doi.org/10.1039/C9CY01519A.

[45] S. Ghosh, T. Ourlin, P.-F. Fazzini, L.-M. Lacroix, S. Tricard, J. Esvan, S. Cayez, B. Chaudret, Magnetically induced $CO_2$ methanation in continuous flow over supported nickel catalysts with improved energy efficiency, ChemSusChem 16 (2023) e202201724, https://doi.org/10.1002/cssc.202201724.

[46] L. Truong-Phuoc, C. Duong-Viet, J.-M. Nhut, A. Pappa, S. Zafeiratos, C. Pham-Huu, Induction heating for the electrification of catalytic processes, ChemSusChem 18 (2025) e202402335, https://doi.org/10.1002/cssc.202402335.

[47] L. Truong-Phuoc, C. Duong-Viet, L. Vidal, T. Romero, J.-M. Nhut, H. Ba, C. Pham, S. Zafeiratos, C. Pham-Huu, Ni/co-decorated silicon carbide foam coated with graphene for dry methane reforming under induction heating, ChemCatChem 18 (2026) e01512, https://doi.org/10.1002/cctc.202501512.